

The nature of the near-infrared interline sky background using fibre Bragg grating OH suppression

Christopher Q. Trinh^{1*}, Simon C. Ellis^{2,1}, Joss Bland-Hawthorn^{1,3}, Anthony J. Horton²,
Jon S. Lawrence^{2,4} and Sergio G. Leon-Saval³

¹*Sydney Institute for Astronomy, School of Physics, The University of Sydney, NSW 2006, Australia*

²*Australian Astronomical Observatory, 105 Delhi Road, North Ryde, P.O. Box 915, NSW 1670, Australia*

³*Institute of Photonics and Optical Science, School of Physics, The University of Sydney, NSW 2006, Australia*

⁴*Department of Physics and Astronomy, Macquarie University, NSW 2109, Australia*

Accepted Received

ABSTRACT

We analyse the near-infrared interline sky background, OH and O₂ emission in 19 hours of *H* band observations with the GNOSIS OH suppression unit and the IRIS2 spectrograph at the 3.9-metre Anglo-Australian Telescope. The observations cover a range of sky positions with varying lunar conditions throughout the night. We find that the temporal behaviour of OH emission is best described by a gradual decrease during the first half of the night followed by a gradual increase during the second half of the night following the behaviour of the solar elevation angle. We measure the interline background at 1.520 μm where the instrumental thermal background is very low and exploit its variation with zenith distance, time after sunset, lunar conditions, and ecliptic latitude to determine the presence of non-thermal atmospheric emission, zodiacal scattered light and scattered moonlight. Zodiacal scattered light is too faint to be detected in the summed observations. Our data are consistent with a contribution from moonlight that is ≈ 30 times greater than expected from a model based on extrapolated *V* band measurements. Demanding near-infrared observations during low lunar phase angles ($|\alpha| \gtrsim 30$ deg) should be made at lunar distances $\rho \gtrsim 80$ deg if the background contribution is not to exceed 100 photons $\text{s}^{-1} \text{m}^{-2} \mu\text{m}^{-1} \text{arcsec}^{-2}$. Although moonlight may dominate the interline background at very small lunar distances, the background at a resolving power of $R \approx 2400$ when using OH suppression fibres is otherwise dominated by light from an atmospheric source that fades gradually throughout the night. As such, it bears a resemblance to atmospheric OH emission suggesting that the interline background contains OH, which likely comes from unsuppressed lines which are scattered into the interline regions by the diffraction grating of the spectrograph. However, the interline background linearly correlates with both OH and O₂ emission, which have different temporal behaviours suggesting it contains contributions from multiple molecular species. The absolute interline background is 560 ± 130 photons $\text{s}^{-1} \text{m}^{-2} \mu\text{m}^{-1} \text{arcsec}^{-2}$ at 1.520 μm under dark conditions. This value is similar to previous measurements without OH suppression suggesting that the suppression with the current grating design does not affect the interline background, likely as a result of poor design due to inaccurate skyline models. Future OH suppression fibre designs will address this issue using more accurate skyline measurements taken from high resolution spectra.

Key words: infrared: general – instrumentation: miscellaneous – instrumentation: spectrographs – atmospheric effects

1 INTRODUCTION

The near-infrared (NIR) background is ≈ 1000 times brighter than the optical background when observing from the ground, severely limiting our ability to observe faint

* E-mail: c.trinh@physics.usyd.edu.au

objects at these wavelengths. For example, even at a good observing site, the typical sky brightness in the H band is $13.8 \text{ mag arcsec}^{-2}$ (Cox 2000) compared to $21.5 \text{ mag arcsec}^{-2}$ in the V band (Krisciunas et al. 1987). From NIR spectra of the night sky it is known that the background is dominated by the bright emission lines associated with the vibrational decay of atmospheric hydroxyl (OH) molecules (Meinel 1950; Dufay 1951). Complicating matters even further, the OH airglow is also known to fluctuate rapidly on short timescales preventing clean subtraction from data (Davies 2007). The situation is rather unfortunate given the importance of the NIR window to the future of cosmology. Thus, overcoming the OH airglow is a fundamental challenge for observational astronomy.

Space-based observations naturally provide a much fainter NIR background. Here the low background consists mainly of zodiacal scattered light and may be as low as ≈ 37.5 to $55 \text{ photons s}^{-1} \text{ m}^{-2} \mu\text{m}^{-1} \text{ arcsec}^{-2}$ in the H band as measured from the $50 \times 50 \text{ arcsec}^2$ Hubble Deep Field-North at an ecliptic latitude, $b = 57 \text{ deg}$ and from the $144 \times 144 \text{ arcsec}^2$ Hubble Ultra Deep Field at $b = -45 \text{ deg}$ using the F160W filter ($\approx 0.4 \mu\text{m}$ bandwidth) of NICMOS on the Hubble Space Telescope (Thompson et al. 2007). In comparison, Maihara et al. (1993) measured an interline sky brightness of $590 \pm 140 \text{ photons s}^{-1} \text{ m}^{-2} \mu\text{m}^{-1} \text{ arcsec}^{-2}$ at $1.665 \mu\text{m}$ in the H band from the ground using the University of Hawaii 2.2-metre telescope on Mauna Kea at a resolving power of $R = 17,000$. More recently, Sullivan & Simcoe (2012) measured $670 \pm 200 \text{ photons s}^{-1} \text{ m}^{-2} \mu\text{m}^{-1} \text{ arcsec}^{-2}$ between 1.662 and $1.663 \mu\text{m}$ using the Folded-port Infrared Echellette (FIRE) spectrometer at Magellan at $R = 6000$. Although the background in space is much dark when compared to the ground, the limited accessibility of space telescopes and the fact that the largest telescope will always be on the ground drives astronomers to continue searching for ways to mitigate the OH airglow from the ground.

Given that the OH lines are intrinsically narrow (Turnbull & Lowe 1983), a low level background from the ground may be possible through OH suppression. It has been demonstrated that the Lorentzian wings of a diffraction grating line profile contributes non-negligible amounts of light from a bright emission line to the interline regions (Bland-Hawthorn et al. 2004; Ellis & Bland-Hawthorn 2008). Recently, Sullivan & Simcoe (2012) claimed that the interline background in their measured H band spectrum was consistent with just scattered OH emission. They compared their observed spectrum to a simulated sky spectrum generated from the OH line list of Rousselot et al. (2000) with Gaussian line profiles ($R = 30,000$) convolved with the measured FIRE line spread function. If this is the case then suppressing the OH lines before any dispersive element should limit the amount of OH light scattered by the diffraction grating into the interline regions and may reduce the interline background by a factor of ~ 40 , which is greater than the reduction resulting from adaptive optics (Ellis & Bland-Hawthorn 2008).

Ellis et al. (2012) and Trinh et al. (2012) attempted to use OH suppression fibres with fibre Bragg gratings (FBGs) designed to suppress the 103 brightest OH doublets in the H band ($1.47 - 1.7 \mu\text{m}$) to demonstrate this. Although the OH suppression fibres demonstrated excellent suppression of the OH lines themselves, no reduction in the interline back-

ground was seen. As a result of the low system throughput, these observations were detector noise-dominated in the interline regions possibly obfuscating the reduction. Alternatively, there may be no reduction due to contributions from unsuppressed OH lines and/or other atmospheric sources and/or astronomical sources. If unsuppressed OH lines are responsible, it may be possible to achieve the desired sensitivity increase by the suppression of more lines. If other atmospheric sources and/or astronomical sources are responsible, these sources may be filterable depending on whether they are line or continuum sources. Thus, understanding the nature of the interline background in the observations made with the first generation of OH suppression fibres is an essential step toward perfecting this technology.

In this paper, we present the analysis of 19 hours of night sky observations in the H band using the GNOSIS OH suppression unit with the IRIS2 imaging spectrograph (Tinney et al. 2004) at the 3.9-metre Anglo-Australian Telescope (AAT). In Section 2, we give a brief description of GNOSIS followed by a description of our observations in Section 3. Section 4 discusses the NIR background sources considered in this study, which includes non-thermal atmospheric emission, zodiacal scattered light and moonlight. We discuss our results in Section 5, which includes an examination of the temporal behaviour of OH emission, a direct comparison of the spatial and temporal behaviours of the interline background with OH and O_2 emission, an assessment of the amount of zodiacal scattered light and moonlight contributing to the interline background as well as a measure of the absolute interline sky brightness during dark time followed by a summary in Section 6.

2 GNOSIS

A detailed description of the GNOSIS OH suppression unit and its performance may be found in Trinh et al. (2012) and Ellis et al. (2012). Here we briefly describe the most important aspects. GNOSIS uses a fore-optics unit containing a 7-element hexagonal lenslet array integral field unit (IFU) mounted at the Cassegrain focus to collect light from the AAT. The hexagonal lenslets are hexagonally packed and span 1.2 arcsec (0.4 arcsec for each lenslet flat-to-flat) on the sky. The light collected by the IFU is transported by a fibre bundle consisting of $50 \mu\text{m}$ core diameter multi-mode fibres (MMFs) to the grating unit.

The grating unit contains 7 OH suppression fibres consisting of two photonic lanterns (Leon-Saval et al. 2005) and two aperiodic FBGs (Bland-Hawthorn et al. 2004). The OH suppression fibres behave like a $50 \mu\text{m}$ core diameter MMF with the spectral response of a single-mode fibre (SMF). The fibres suppress the 103 brightest OH doublets in the range $1.47 - 1.7 \mu\text{m}$ using deep (up to 40 dB depending on the line strength) and narrow ($R \approx 10,000$) notches while maintaining relatively high throughput between the notches for scientific observations ($\approx 60\%$ at $1.55 \mu\text{m}$).

The grating unit passes the OH suppressed light to the IRIS2 spectrograph via a $\approx 10 \text{ m}$ long fibre bundle for measurement. The fibre bundle is terminated in a linear pseudo-slit mounted in an interface unit positioned over the IRIS2 dewar window. An optical relay within the interface unit images the pseudo-slit onto the IRIS2 slit plane with a

Table 1. Night sky observations made with GNOSIS with IRIS2 at the AAT. Symbol definitions are as follows: t_{exp} - exposure time, t - time after sunset, z - zenith distance, l - longitude, b - latitude, ρ - lunar distance, α - lunar phase angle.

No.	Date	t_{exp} (s)	t (hr)	Sky			Ecliptic		Moon		
				Local z (deg)	Galactic l (deg)	b (deg)	l (deg)	b (deg)	ρ (deg)	z (deg)	α (deg)
1	1 Sept. 2011	1800	5.55	6.74	27.29	-59.64	330.63	-15.81	120.76	111.73	-131
2	1 Sept. 2011	1800	6.06	37.18	27.29	-59.64	330.63	-15.81	120.76	116.94	-131
3	1 Sept. 2011	1800	8.66	43.63	27.29	-59.64	330.63	-15.81	120.76	134.09	-131
4	1 Sept. 2011	1800	9.16	10.16	27.29	-59.64	330.63	-15.81	120.75	134.49	-131
5	1 Sept. 2011	1800	10.74	11.19	246.08	-53.73	33.84	-57.56	118.19	128.58	-131
6	1 Sept. 2011	1800	11.25	48.90	246.08	-53.73	33.83	-57.56	118.19	124.80	-131
7	2 Sept. 2011	1800	1.29	51.76	332.20	36.64	221.84	-5.42	2.31	46.12	-119
8	2 Sept. 2011	1800	2.31	7.82	338.67	28.10	231.91	-7.00	10.91	59.14	-119
9	2 Sept. 2011	1800	3.23	24.38	7.61	-20.24	288.32	-8.90	66.46	70.94	-119
10	2 Sept. 2011	1800	4.11	18.93	36.41	-57.87	332.05	-10.96	109.33	81.93	-119
11	2 Sept. 2011	1800	7.16	34.71	27.34	-59.63	330.64	-15.78	107.31	115.77	-119
12	2 Sept. 2011	1800	8.40	41.17	27.26	-59.62	330.61	-15.82	107.28	125.33	-119
13	2 Sept. 2011	1800	8.90	64.65	27.26	-59.62	330.61	-15.82	107.28	127.96	-119
14	2 Sept. 2011	1800	10.76	33.15	27.29	-59.64	330.63	-15.81	107.30	129.13	-119
15	3 Sept. 2011	1800	3.22	26.69	27.29	-59.64	330.63	-15.81	93.98	57.97	-105
16	3 Sept. 2011	1800	3.72	7.93	27.29	-59.64	330.63	-15.81	93.98	64.37	-105
17	3 Sept. 2011	1800	6.11	13.14	27.29	-59.64	330.63	-15.81	93.98	93.33	-105
18	3 Sept. 2011	1800	6.61	33.44	27.29	-59.64	330.63	-15.81	93.98	98.95	-105
19	3 Sept. 2011	900	8.67	32.84	154.71	-57.52	27.68	-10.06	149.40	118.47	-105
20	3 Sept. 2011	900	8.92	33.42	154.71	-57.52	27.68	-10.06	149.40	120.28	-105
21	3 Sept. 2011	900	9.69	34.39	154.71	-57.52	27.68	-10.06	149.40	124.69	-105
22	3 Sept. 2011	900	9.95	51.78	154.71	-57.52	27.68	-10.06	149.40	125.73	-105
23	4 Sept. 2011	900	4.37	49.57	90.63	-48.78	356.16	11.24	106.22	60.16	-92
24	4 Sept. 2011	900	4.62	36.45	90.63	-48.78	356.16	11.24	106.22	63.35	-92
25	4 Sept. 2011	900	5.78	35.19	88.21	-55.56	355.40	4.34	105.63	77.71	-92
26	4 Sept. 2011	900	6.03	28.50	88.21	-55.56	355.40	4.34	105.63	80.76	-92
27	4 Sept. 2011	1800	7.77	34.97	27.27	-59.63	330.62	-15.81	80.93	100.44	-92
28	4 Sept. 2011	1800	8.27	36.94	27.27	-59.63	330.62	-15.81	80.93	105.58	-92
29	4 Sept. 2011	900	10.33	38.76	154.71	-57.52	27.68	-10.06	136.69	121.83	-92
30	4 Sept. 2011	900	10.59	47.53	154.71	-57.52	27.68	-10.06	136.69	123.08	-92
31	4 Sept. 2011	900	11.54	4.28	154.71	-57.52	27.68	-10.06	136.69	125.78	-92
32	5 Sept. 2011	1800	0.48	49.45	353.78	5.13	259.21	-8.29	9.54	9.04	-80
33	5 Sept. 2011	900	1.92	46.23	27.27	-59.63	330.62	-15.81	68.29	17.69	-80
34	5 Sept. 2011	900	2.17	31.68	27.27	-59.63	330.62	-15.81	68.29	20.72	-80
35	5 Sept. 2011	900	3.31	28.42	27.27	-59.63	330.62	-15.81	68.29	35.04	-80
36	5 Sept. 2011	900	3.56	18.59	27.27	-59.63	330.62	-15.81	68.29	38.29	-80
37	5 Sept. 2011	900	4.33	5.68	27.27	-59.63	330.62	-15.81	68.29	48.20	-80
38	5 Sept. 2011	900	5.62	6.12	27.27	-59.63	330.62	-15.81	68.29	64.55	-80
39	5 Sept. 2011	900	5.87	26.47	27.27	-59.63	330.62	-15.81	68.29	67.72	-80
40	5 Sept. 2011	900	7.65	29.72	27.29	-59.63	330.63	-15.81	68.30	89.16	-80
41	5 Sept. 2011	900	7.90	42.90	27.29	-59.63	330.63	-15.81	68.30	92.04	-80
42	5 Sept. 2011	900	8.93	46.13	27.29	-59.63	330.63	-15.81	68.30	103.10	-80
43	5 Sept. 2011	900	9.18	57.88	27.29	-59.63	330.63	-15.81	68.30	105.63	-80
44	5 Sept. 2011	900	10.11	61.05	27.29	-59.63	330.63	-15.81	68.30	114.06	-80
45	5 Sept. 2011	900	10.37	30.35	27.29	-59.63	330.63	-15.81	68.30	116.06	-80

PSF FWHM of ≈ 2 pixels resulting in a resolving power of $R \approx 2350$ and a dispersion of $\approx 3.5 \text{ \AA pix}^{-1}$. IRIS2 contains a 1024×1024 Rockwell Hawaii-1 detector with a dark current of $\approx 0.015 \text{ e}^- \text{ s}^{-1}$ and an effective read noise of $\approx 8 \text{ e}^-$ when using multiple read mode. For GNOSIS observations IRIS2 is configured with a custom slit mask with $250 \mu\text{m}$ diameter holes and a f/12 cold stop. The total throughput of the system including telescope, GNOSIS, and IRIS2 was ≈ 4 per cent for a diffuse source.

3 OBSERVATIONS

A total of 19 hours of H band observation were taken between 1 – 5 September 2011 in multiple read mode (MRM) to minimise read noise. 45 separate frames were taken with exposure times of either 30 (61 reads, 30 s period) or 15 (61 reads, 15 s period) minutes. Table 1 lists the details of each observation. The observations made on 1 – 4 September included 6 OH suppression fibres and 1 control (unsuppressed) fibre.

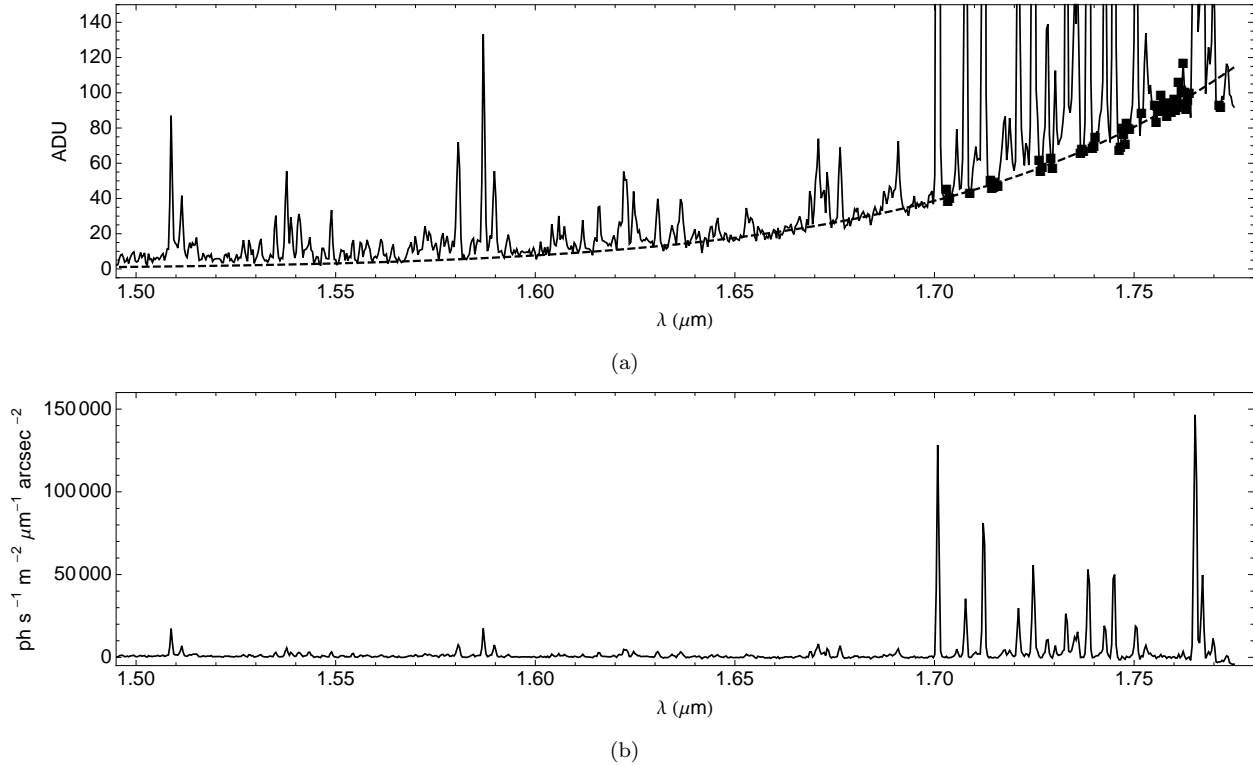


Figure 1. (a) The dark-subtracted OH suppressed spectrum of sky frame 1 in Table 1. The squares show the continuum points used to fit a black-body spectrum and the dashed line shows the best-fitting black-body spectrum. (b) The dark-subtracted, thermal-subtracted and flux-calibrated OH suppressed spectrum of sky frame 1.

3.1 Data Reduction

We utilise a data reduction procedure similar to the general data reduction procedure for GNOSIS data given in Ellis et al. (2012). Here we give a brief summary of the data reduction procedure used specifically for the night sky observations. For each MRM sky frame all 61 reads were saved. There was a significant non-linearity in the detector response in the first few reads so we dropped the first 5 reads from the linear least squares fit when constructing the final image. Then, the image was corrected for detector non-linearity due to the filling of the pixel wells by the procedure given on the IRIS2 web pages.¹

The 7 spectra were spread across 2 detector quadrants. We noticed that despite using MRM, the median count level along the spectral direction computed from 200 spatial pixels at each spectral pixel in the un-illuminated portion of the detector showed a discontinuity in between the 2 quadrants and some slow-varying structure within each quadrant. We used this as our measure of dark current and subtracted it from each detector row.

The dark-subtracted sky spectrum in each fibre was extracted using the “Gaussian summation extraction by least squares” method of Sharp & Birchall (2010) using traces defined from a spectroscopic observation of the dome flat lamp. Spectroscopic observations of the dome flat lamp on each night were also used to determine the fibre-to-fibre throughput variation. The dome flat lamp spectrum in each fibre

was extracted, integrated and normalised to the mean of all 7 fibres. The extracted sky spectra were divided by these relative throughput values.

A wavelength calibration was obtained for each fibre from a xenon arc lamp observation. In the xenon arc lamp spectrum in each fibre a cubic polynomial was fitted to pixel position of each xenon line.

The OH suppressed spectra were combined by taking the median of the 6 (1 – 4 September) or 7 (5 September) spectra at each spectral pixel, which removes cosmic ray hits and other artefacts. The wavelength solution for the central sky fibre was applied to the median-combined OH suppressed spectra. This results in an accuracy of $\approx 2 \text{ \AA}$ due to the slight shift in the wavelength solution from fibre to fibre.

The thermal background was removed from each spectrum by fitting a black-body spectrum with an emissivity of $\epsilon = 1$ to the continuum values at $\lambda > 1.7 \mu\text{m}$ using FINDFIT in MATHEMATICA and subtracting the best-fitting model. The functional form of the black-body spectrum in units of photons $\text{s}^{-1} \text{m}^{-2} \mu\text{m}^{-1} \text{arcsec}^{-2}$ is

$$N_{\text{bb}}(\lambda, T, \epsilon) \approx \frac{1.41 \times 10^{16} \epsilon}{\lambda^4 \left[\exp\left(\frac{14387.7}{\lambda T}\right) - 1 \right]}, \quad (1)$$

where λ is the wavelength in μm , and T is the temperature. Most of the thermal background comes from the slit block in the IRIS2 interface unit and we converted the black-body spectrum from photons $\text{s}^{-1} \text{m}^{-2} \mu\text{m}^{-1} \text{arcsec}^{-2}$ to ADU assuming a throughput of 11.4 per cent, which includes a 5 per cent loss from slit block alignment and 12 per cent through-

¹ http://www.aao.gov.au/AAO/iris2/iris2_linear.html

put for IRIS2 (Ellis et al. 2012). Figure 1a shows the OH suppressed spectrum from sky frame 1 in Table 1 with the best-fitting black-body model shown by the dashed curve and the continuum points used to compute the best-fitting model shown by squares.

Next, the sky spectra were divided by the instrument response, which corrects for variation in throughput with wavelength and telluric features. The instrument response was measured from a sky-subtracted A0V standard star observation. The stellar spectrum in each fibre was divided by a model spectrum of Vega (Castelli & Kurucz 1994) and normalised to the mean value between 1.5 – 1.69 μm .

Lastly, the sky spectra were flux-calibrated assuming an efficiency of 4 per cent based on throughput measurements of GNOSIS, IRIS2, and estimates of the AAT (Ellis et al. 2012; Trinh et al. 2012). Figure 1b shows the dark-subtracted, thermal-subtracted, flux-calibrated OH suppressed spectrum from sky frame 1.

4 INTERLINE BACKGROUND SOURCES

Below we discuss the main NIR interline background sources, which include non-thermal atmospheric emission (OH and other molecules), zodiacal scattered light and scattered moonlight. Other contributions, such as zodiacal emission from interplanetary dust at the ecliptic plane, Galactic dust emission from interstellar dust and the cosmic microwave background are negligible in the H band (Ellis & Bland-Hawthorn 2008). Thermal emission was removed as fully as possible during our data reduction.

4.1 Atmospheric emission

The interline background is likely to contain a strong atmospheric component that may be composed of OH light scattered by the diffraction grating of the spectrograph, either from suppressed or unsuppressed OH lines and/or emission from other atmospheric molecules. The temporal behaviour of such molecular emission arises from physical processes that affect that reactions rates between atmospheric molecules. The emission intensity varies spatially due to the airmass. As such, the temporal and spatial parts are independent and the emission from an atmospheric molecule may be written as

$$I(t, z) = I_0(t)X(z), \quad (2)$$

where t is the time after sunset, $I_0(t)$ is the time-dependent intensity specific for each atmospheric molecule, z is the zenith distance and $X(z)$ is the optical path or airmass.

For OH emission emitted from a layer at height $h \approx 87$ km (Baker & Stair 1988), the optical path is given by the van Rhijn factor (van Rhijn 1921)

$$X_1(z) = \left[1 - \left(\frac{R}{R+h} \right)^2 \sin^2 z \right]^{-1/2}, \quad (3)$$

where R is the radius of the Earth. For more general atmospheric emission where the emitting height is unknown, the optical path is given by the standard expression

$$X_2(z) = \sec(z). \quad (4)$$

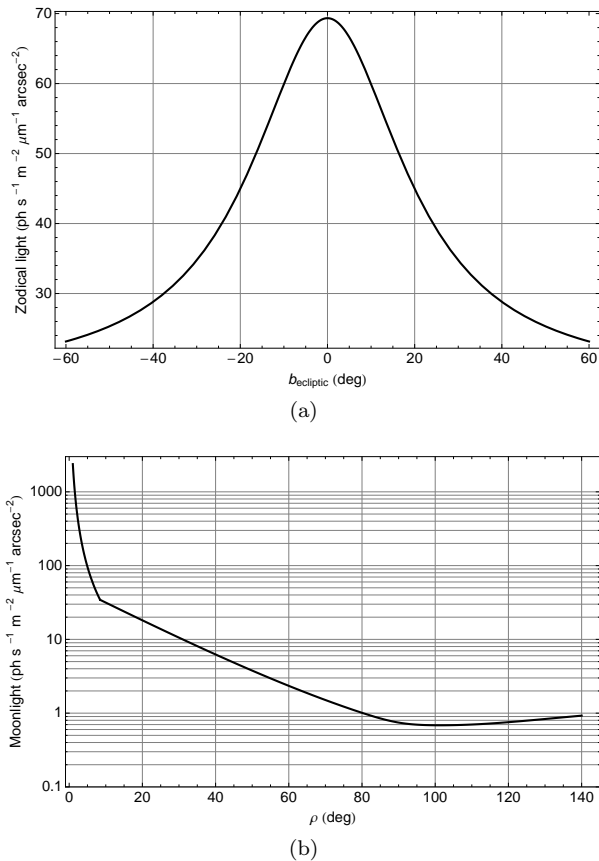


Figure 2. (a) The zodiacal scattered light model from Ellis & Bland-Hawthorn (2008) based on J band measurements from Kelsall et al. (1998) with a $T = 5800$ K and $\epsilon = 1.08 \times 10^{-13}$ black-body spectrum. (b) The scattered moonlight model extrapolated from the V band measurements of Krisciunas & Schaefer (1991) using the wavelength dependence of Rayleigh and Mie scattering for $\lambda = 1.520 \mu\text{m}$, $\alpha = -80$ deg, $z_{\text{sky}} = 0$ deg, and $z_{\text{moon}} = \rho$.

Excited OH radicals are primarily created by a reaction between hydrogen and ozone (Bates & Nicolet 1950)



and may be quenched by reactions such as (Llewellyn et al. 1978)



The temporal behaviour of OH emission varies on both short and long time-scales due to physical processes that affect these chemical reactions. On short time-scales, OH intensity fluctuates by ≈ 15 per cent over periods of 15 minutes (Taylor et al. 1991) to 1 hr (Yee et al. 1991) due to gravity waves (Ramsay et al. 1992; Frey et al. 2000) that induce density and temperature perturbations.

On long time-scales, OH intensity decreases throughout the night by a factor of 2-3 (Ramsay et al. 1992; Content 1996; Glazebrook & Bland-Hawthorn 2001) due to changes in the altitude-number density profiles of the minor atmospheric constituents as a result of the lack of sunlight (Shimazaki & Laird 1970). The long-term decline of OH emission through the night is typically modelled as linear (Content 1996; Sullivan & Simcoe 2012).

Table 2. Linear models for the temporal behaviour of OH emission.

Date	Mean OH (photons s ⁻¹ m ⁻² μm ⁻¹ arcsec ⁻²)	OH RMS (per cent)	Slope	Slope error	Intercept	Intercept error	R ²
1 Sept 2011	55050	21	0.07	0.03	0.4	0.30	0.535
2 Sept 2011	65200	21	-0.05	0.02	1.3	0.12	0.526
3 Sept 2011	66400	11	0.01	0.02	0.9	0.13	0.090
4 Sept 2011	52300	8	-0.01	0.01	1.1	0.09	0.106
5 Sept 2011	64800	13	-0.03	0.06	1.2	0.01	0.443
All	60700	18	-0.014	0.007	1.09	0.05	0.080
All (< 7.5 hr)			-0.07	0.01	1.31	0.05	0.628
All (> 7.5 hr)			0.07	0.02	0.19		0.309

4.2 Zodiacal scattered light

A large component of the interline background in space-based observations is zodiacal scattered light (ZSL), which comes from sunlight scattering off interplanetary dust. With OH suppression, ground-based observations may be sensitive enough to detect ZSL. Kelsall et al. (1998) provided a model for ZSL at 1.25 μm as a function of ecliptic latitude. For the *H* band, Ellis & Bland-Hawthorn (2008) utilised an analytic approximation to the Kelsall et al. (1998) model with a $T = 5800$ K and $\epsilon = 1.08 \times 10^{-13}$ black-body spectrum, i.e.,

$$I_{\text{ZSL}}(b) = I_{0,\text{ZSL}} N_{\text{bb}}(\lambda, T, \epsilon) \left\{ \frac{0.75}{[1 + (2b/0.743)^2]} + 0.25 \right\}, \quad (7)$$

where we have included $I_{0,\text{ZSL}}$ as an overall scaling constant. Figure 2a shows the Ellis & Bland-Hawthorn (2008) ZSL model with $I_{0,\text{ZSL}} = 1$, which gives ≈ 70 photons s⁻¹ m⁻² μm⁻¹ arcsec⁻² near the ecliptic plane.

4.3 Scattered moonlight

It is well-known that scattered moonlight contributes significantly to the sky background in the optical. We adapted the model of Krisciunas & Schaefer (1991), which is based on measurements in the *V* band, to the *H* band using the wavelength dependence of Rayleigh and Mie scattering as described in the Canada France Hawaii Telescope (CFHT) Redeye manual.² The contribution from scattered moonlight varies as function of wavelength, lunar phase angle (α), lunar zenith distance (z_{moon}), the zenith distance of the sky position (z_{sky}), the angular distance between the Moon and the sky position or lunar distance (ρ) and the atmospheric extinction (k) as

$$B = I(\alpha) f(\rho, \lambda) 10^{-0.4k X_3(z_{\text{moon}})} [1 - 10^{-0.4k X_3(z_{\text{sky}})}]. \quad (8)$$

B is in the units of nanolamberts.

The first term, $I(\alpha)$ is the intensity of moonlight as a function of phase angle in degrees and has the form

$$I(\alpha) = 10^{-0.4[3.84 + 0.026|\alpha| + (4 \times 10^{-9})\alpha^4 - 1.3]}. \quad (9)$$

The function is symmetric and sharply peaked about $\alpha = 0$, which corresponds to full moon.

The second term, $f(\rho, \lambda)$ is the scattering function, which contains both Rayleigh and Mie scattering contributions. Including the typical Rayleigh and Mie scattering wavelength dependences in the empirical *V* band scattering functions measured over Mauna Kea by Krisciunas & Schaefer (1991) yields

$$f(\rho, \lambda) = \begin{cases} 6.2 \cdot 10^7 \rho^{-2} \left(\frac{0.55}{\lambda}\right)^{1.3} & \rho < 8.5 \\ 10^{6.15 - \rho/40} \left(\frac{0.55}{\lambda}\right)^{1.3} + 2.27 \cdot 10^5 (1.06 + \cos^2 \rho) \left(\frac{0.55}{\lambda}\right)^4 & \rho \geq 8.5 \end{cases}, \quad (10)$$

where λ is in μm and ρ is in degrees. The function rises steeply at $\rho \lesssim 10$ deg.

The moonlight must travel through an optical path length of $X_3(z_{\text{moon}})$ before being scattered by the patch of sky being observed. Here the optical path is given by

$$X_3(z) = (1 - 0.96 \sin^2 z)^{-0.5}. \quad (11)$$

Then the scattered moonlight must travel through an optical path length of $X_3(z_{\text{sky}})$ to reach the detector. The latter terms in Equation 8 describes the dependence on these two quantities.

Equation 8 may be converted to the units of mag arcsec⁻² by (Garstang 1989)

$$V = \frac{20.7233 - \ln(B/34.08)}{0.92104}. \quad (12)$$

The final *H* band moonlight contribution is given in photons s⁻¹ m⁻² μm⁻¹ arcsec⁻² by

$$I_{\text{moon}}(\lambda, \rho, \alpha, z_{\text{moon}}, z_{\text{sky}}) = I_{0,\text{moon}} \frac{27.040 \times 10^{(20-V)/2.5}}{0.290}, \quad (13)$$

where we have include $I_{0,\text{moon}}$ as an overall scaling constant. Figure 2b shows the *H* band moonlight contribution for $\lambda = 1.520$ μm, $\alpha = -80$ deg, $z_{\text{sky}} = 0$ deg, $z_{\text{moon}} = \rho$ and $I_{0,\text{moon}} = 1$. $\alpha = -80$ deg is the largest lunar phase angle in our data set and we only expect appreciable amounts of moonlight at very small lunar distances.

5 RESULTS

5.1 OH emission temporal behaviour

We begin by investigating the temporal behaviour of OH emission in order to obtain an empirical model to analyse the interline background. We measured the OH emission intensity in the suppressed spectrum of each sky frame by measuring 17 OH lines that were beyond the suppression

² <http://www.cfht.hawaii.edu/Instruments/Detectors/IR/Redeye/Manual/chapter7.html>

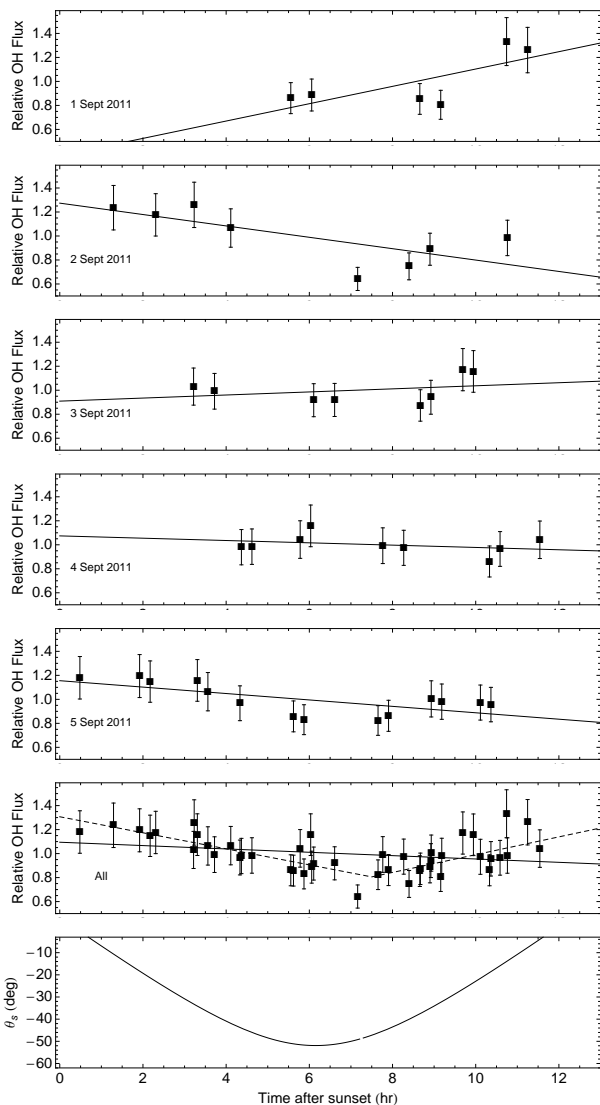


Figure 3. The temporal behaviour of OH emission for 1 – 5 September 2011. The values have been corrected to an airmass of unity by dividing by the van Rhijn factor and normalised to the mean value on each night. The error bars represent the 15 per cent short time-scale fluctuations in OH emission due to gravity waves. The solid line shows the best-fitting linear model. The bottom panel shows the solar elevation angle (θ_s) on the night of 5 September 2011. OH emission intensity appears to begin increasing after θ_s reaches a minimum at ≈ 7 hr after sunset. The dashed line shows a piecewise linear model where the first half of the night (< 7.5 hr) is treated separately from the second half and provides a better fit to the data compared to the simple linear model.

range at $\lambda > 1.7 \mu\text{m}$ (see Figure 1b). The OH lines do not vary in unison; only lines within the same vibrational transitions will be correlated. As such, we used the mean peak value of the OH lines as the measure of OH emission intensity in each sky frame.

Figure 3 shows the temporal behaviour, $I_0(t)$, of OH emission for each night between 1 and 5 September 2011. The spatial dependence has been removed by dividing by $X_1(z)$. Additionally, the intensities have been normalised to the mean intensity on each individual night, which are

listed in Table 2. As expected, the temporal behaviour of OH emission is not simple. There are large fluctuations and the pattern is different from night to night. The RMS values for each night vary from 8 to 21 per cent and are listed in Table 2. The RMS of the mean OH emission on each night was 12 per cent and the total RMS over all nights was 18 per cent.

The time curves for 2 and 5 September 2011 show the OH emission during the first half of the night being greater than the second half, in agreement with previous observations (Ramsay et al. 1992; Content 1996; Glazebrook & Bland-Hawthorn 2001). On the other hand, the time curves for 3 and 4 September 2011 are more level, but contain few sample points very early in the night when OH emission is the greatest. For each individual night as well as the aggregate of all 5 nights, we used `LINEARMODELFIT` in `MATHEMATICA` to determine the best-fitting slope and intercept. The standard error for each free parameter was computed from the covariance matrix. The best-fitting parameters, their standard errors and the coefficient of determination for each night are listed in Table 2.

Although the temporal behaviour of OH emission is typical described by a simple linear model there appears to be a minimum near 7 hr after sunset and a subsequent rise in intensity, a trend which the monotonically decreasing linear model does not capture. This rise in intensity later in the night may be a similar effect to the exponential rise in geocoronal H α due to solar Ly β excitation of neutral hydrogen in the exosphere at a height of 500 km (Bland-Hawthorn et al. 1998). The increase in H α begins ≈ 6 hr before sunrise as the amount of sunlight reaching the exosphere increases with increasing solar elevation angle (θ_s). OH emission comes from an emitting layer in the mesosphere at ≈ 90 km and it is plausible that it too increases as twilight ends due to increasing solar irradiation. To confirm this, we computed the solar elevation angle for the night of 5 September 2011, which is shown in bottom panel of Figure 3. Comparing the aggregate OH emission data with the solar elevation, the intensity is minimum near the minimum solar elevation angle at ≈ 7 hr after sunset and the intensity rises after this time coincides with an increase in solar elevation angle. Thus, a function that follows the behaviour of $\theta_s(t)$ is probably best suited to describing the OH emission intensity as a function of time.

Fitting linear models separately to the first and second halves of the night gives a function with this behaviour. The slope and intercepts of this piecewise linear model are listed in Table 2 and shown by the dashed line in Figure 3. The intercept of the linear model for the second half of the night is constrained to be continuous with the linear model for the first half of the night at 7.5 hr (which provides the best fit to the data). Simply comparing the R^2 values demonstrates that the piecewise linear model gives a better description of the temporal behaviour of OH emission than the simple monotonically declining linear model and we use this model below in our analysis of the ILB.

5.2 Interline background

Now that we have analysed the temporal behaviour of OH emission, we determine the nature of the interline background (ILB). First, we directly compare the spatial and

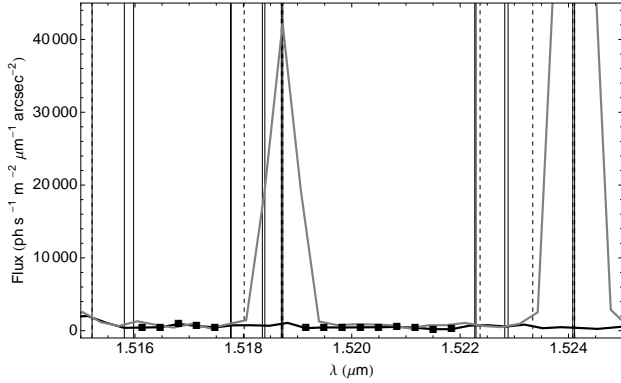


Figure 4. The suppressed (black) and unsuppressed (gray) spectra of sky frame 1 with the points used in the ILB measurements shown by squares. The vertical lines show the OH lines from Rousselot et al. (2000) and the dashed lines show the OH lines from Abrams et al. (1994).

temporal behaviour of the ILB to that of OH and O₂ to determine if the ILB contains an atmospheric component. Both OH and O₂ exhibit similar $X(z)$ dependence as both are atmospheric emission sources (but have different temporal behaviour early in the night). Then, we exploit the ILB variability with lunar conditions and ecliptic latitude to determine the contribution from non-atmospheric sources.

Maihara et al. (1993) measured the ILB at 1.665 μm between two OH lines at 1.66111 and 1.66925 μm. In our data, this region is dominated by instrumental thermal background (see Figure 1a) making it difficult to assess the sky brightness at this wavelength. We selected a region near 1.520 μm where the instrumental thermal background is very low. Specifically, we used the regions from 1.5160 to 1.5175 and 1.5190 to 1.5225 μm, which are near a suppressed OH line at 1.51871 μm but do not coincide with this suppressed line or any other unsuppressed OH lines that appear in the line lists of Rousselot et al. (2000) or Abrams et al. (1994).

The suppressed (black) and unsuppressed (gray) spectra of sky frame 1 are shown in Figure 4 with the points used for the ILB measurement shown by squares. The OH lines according to Rousselot et al. (2000) and Abrams et al. (1994) are shown by the solid and dashed vertical lines, respectively. We took the ILB to be the mean flux in the two regions. The uncertainty in the ILB was obtained from the variation in the individual 6 (1 – 4 September) or 7 (5 September) OH suppressed fibres. Specifically, uncertainty is the standard deviation of the median flux in the two regions in each fibre.

Our assessment of O₂ emission comes from the a-X v=1-0 emission line at 1.58 μm. We measured the peak value of the emission line in the suppressed spectrum of each sky frame.

5.2.1 Non-thermal atmospheric component

In this section, we demonstrate that the ILB contains a strong atmospheric component by directly comparing the spatial and temporal behaviour of the ILB to that of OH and O₂ emission. It is plausible that the ILB contains OH scattered by the diffraction grating of the spectrograph given

the presence of OH lines near the ILB measurement region. The HITRAN2008 models (Rothman et al. 2009) from SpectralCalc.com show 28, 106, 28, 30, 80, 15, and 46 transitions between 1.516 and 1.518 μm for H₂O, CO₂, N₂O, CH₄, NO, OH and C₂H₂, respectively. Between 1.519 and 1.523 μm the model shows 59, 234, 18, 48, 210, 43 and 148 transitions for those same species. Thus, O₂ is unlikely to directly contribute to the ILB, but the ILB may contain contributions from any one of these molecules which may have a temporal behaviour similar to O₂.

We simplify Equation 2 to a single variable by only considering 13 sky frames of the same field (RA = 338.839 deg, dec = -25.953 deg), which we will refer to as field A from here on, taken throughout the night of 5 September 2011 as field A rises and sets. In this case, the zenith distance is a simple function of time after sunset given by

$$\cos z(t) = \sin \delta_A \delta_{\text{SSO}} + \cos \delta_A \cos \delta_{\text{SSO}} \cos[\alpha_A - \alpha_{\text{SSO}}(t)], \quad (14)$$

where (α_A, δ_A) and $(\alpha_{\text{SSO}}(t), \delta_{\text{SSO}})$ are the right ascension and declination of the field A and zenith at Siding Spring Observatory at the time of observation, respectively, and $\alpha_{\text{SSO}}(t)$ is a simple linear function with time. Hence, the emission intensity is only a function of time after sunset, i.e.,

$$I(t) = I_0(t)X[z(t)]. \quad (15)$$

A quick examination of Equations 3, 4 and 11 shows that $X[z(t)]$ monotonically decreases to a minimum as field A rises ($z(t)$ decreasing) during the first half of the night and $X[z(t)]$ monotonically increases as field A sets ($z(t)$ increasing) during the second half of the night. This behaviour readily distinguishes an atmospheric source from non-atmospheric sources and we examine if the ILB follows this sort of curve to establish whether or not it is atmospheric in nature.

Figure 5 shows the OH (top) and O₂ (middle) emission and the ILB (bottom) as a function of time after sunset. The line shows the $I(t)$ curve for an atmospheric source when following a rising and setting field with constant $I_0(t)$ and with $X = X_1$ for OH and $X = X_2$ for O₂. The $I_0(t)$ values have been determined by eye. Both OH and O₂ exhibit the expected $X[z(t)]$ behaviour, monotonically decreasing to a minimum and monotonically increasing during the second half of the night. The data do not exactly follow the curve, but this is expected as neither OH or O₂ are truly constant $I_0(t)$ sources. OH shows elevated emission both early and late in the night due to mechanisms discussed in Section 4.1 and O₂ shows a very rapid dimming after sunset.

The ILB behaviour is very similar to the behaviour of OH and O₂ emission suggesting that the ILB has a strong atmospheric component. In fact, the only plausible explanation for the observed ILB trend with time after sunset is an atmospheric emission source that varies according to $X[z(t)]$ (assumed to be X_2), but with elevated emission early in the night due to an $I_0(t)$ term for the specific molecule(s) responsible for the ILB. ZSL is constant with time after sunset given that the ecliptic latitude for field A is fixed in this set of observations. Scattered moonlight varies with $X_3[z(t)]$, but this component is much too weak (see Section 5.2.3) to account for the observed ILB intensity. Also, the moonlight component depends on lunar zenith distance, which is monotonically increasing as a function of time after sunset and would lead to the scattered moonlight intensity being

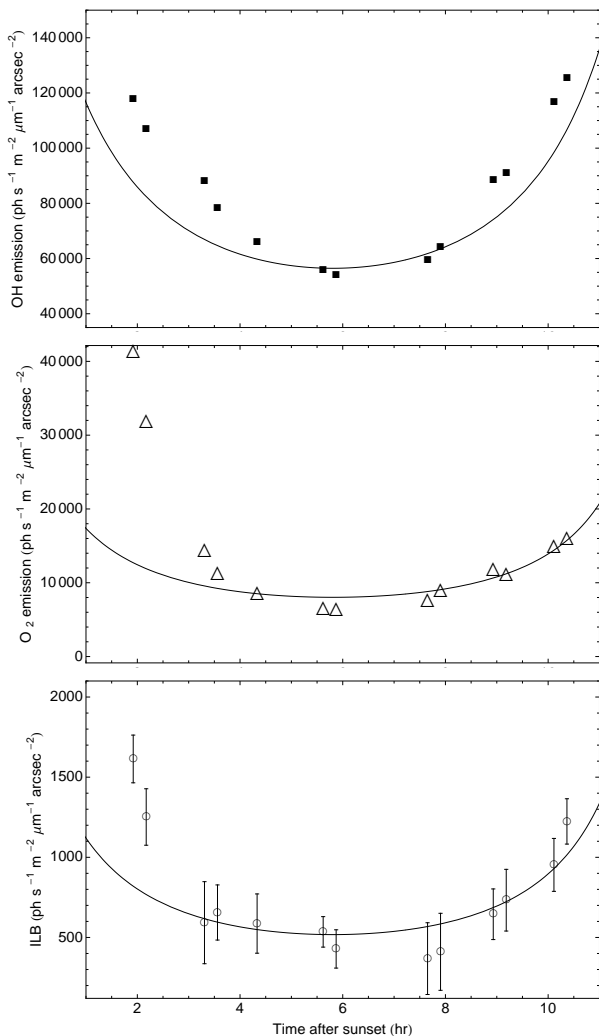


Figure 5. OH (top) and O₂ (middle) emission and the interline background (bottom) as a function of time after sunset from 13 observations taken on 5 September 2011 following field A as it rises and sets. The line shows the $I(t)$ curve for an atmospheric source when following a rising and setting field with constant $I_0(t)$ (determined by eye) and with $X = X_1$ for OH and $X = X_2$ for O₂ and the interline background. OH, O₂ and the interline background are not truly constant $I_0(t)$ sources, which explains the deviations from the $I(t)$ curves. Regardless, the characteristic $X[z(t)]$ behaviour for an atmospheric source when following a rising and setting field is clearly visible.

higher at the end of the night in opposition to what is seen in Figure 5. Thus, we conclude that the ILB is certainly dominated by emission from atmospheric molecules.

Next, we corrected the ILB for the $X_2[z(t)]$ dependence and investigated the $I_0(t)$ behaviour of the ILB making direct comparisons with $I_0(t)$ for OH and O₂ emission for more clues on the origin of the atmospheric component. Figure 6 shows the airmass-corrected OH (squares) and O₂ (triangles) emission intensities normalised to the mean intensity for the night as a function of time after sunset. Also shown are the airmass-corrected ILB intensity (circles) normalised to the mean ILB intensity for the night.

The temporal behaviour of the airmass-corrected ILB closely follows OH, which suggests that the ILB contains

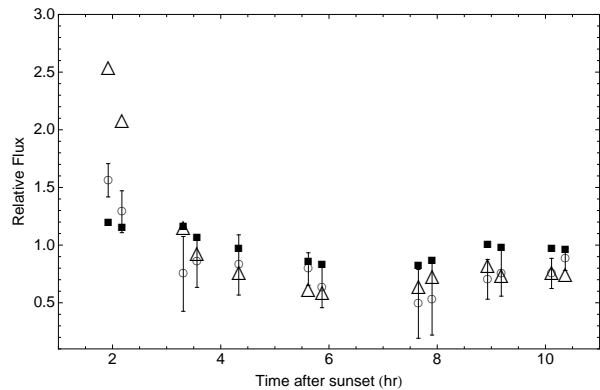


Figure 6. The airmass-corrected OH (squares) and O₂ (triangles) emission intensities and the interline background (circle) as a function of time after sunset normalised to the mean intensity for the 13 observations of field A on the night of 5 September 2011. Late in the night, the temporal behaviour of the interline background is similar to both OH and O₂. Early in the night, the dimming of the interline background is intermediate between the rapid rate of O₂ and the slow rate of OH suggesting contributions from multiple atmospheric molecules with different dimming rates early in the night.

OH as anticipated. However, early in the night, the ILB dims more rapidly than OH. O₂ and other molecules with similar temporal behaviour dim even more rapidly than ILB and OH early in the night. The the ILB is intermediate between the slow rate of OH and the fast rate of O₂ (and like molecules), which suggest that the ILB contains contributions from multiple molecules with different dimming rates early in the night.

To investigate further we determined the linear correlation between the ILB and OH and O₂ emission instead of comparing the behaviour through the night. For this purpose, we considered all 27 observations of field A because the night to night variation of OH or O₂ emission should simply result in a corresponding variation in the ILB if the quantities are correlated. The ZSL contribution to the ILB should be identical in all these frames and the moonlight contribution is small and varies by $\lesssim 30$ photons $s^{-1} m^{-2} \mu m^{-1} arcsec^{-2}$ from frame to frame based on best estimate of moonlight from Section 5.2.3.

Figure 7 shows the airmass-corrected ILB versus OH (left) and O₂ (right) emission for all observations of field A with the best-fitting slope and intercept and their standard errors determined using LINEARMODELFIT in MATHEMATICA. The best-fitting linear correlation for OH has a slope of 0.009 ± 0.002 and intercept of 0 ± 140 with $R^2 = 0.397$. The best-fitting linear correlation for O₂ has a slope of 0.028 ± 0.003 and intercept of 280 ± 40 with $R^2 = 0.736$. Thus, the ILB correlates with both OH and O₂. This corroborates the conclusion above that the ILB contains contributions from multiple atmospheric molecules with temporal behaviour like OH and like O₂. It is not possible for us to make a positive identification of which atmospheric molecules contribute to the ILB with the present analysis. Doing so would require high resolution, high sensitivity spectra of the region where the ILB was measured. However, it is certainly plausible that the ILB contains OH, given the

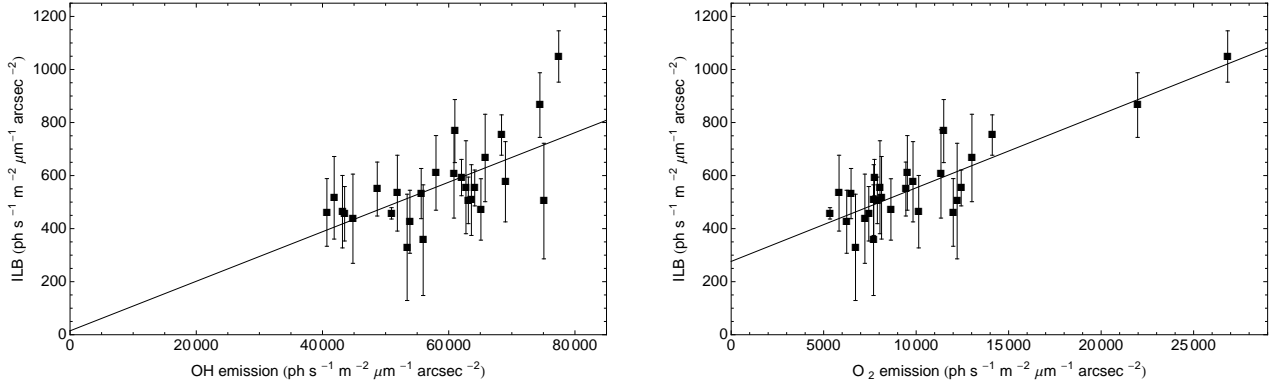


Figure 7. The interline background versus OH (left) and O₂ (right) emission for 27 sky frames of field A. All values have been adjusted to an airmass of unity. The interline background linearly correlates with both OH and O₂ suggesting that the strong atmospheric component in the interline background contains contributions from multiple molecules with temporal behaviours like OH and O₂. The expected contributions from moonlight and ZSL in these frames is very low and should not significantly affect the linear correlation.

prevalence of OH transitions near the region where the ILB was measured, but there are also contributions from other atmospheric molecules with a similar temporal behaviour as O₂.

5.2.2 Zodiacal scattered light

Above, we have demonstrated that the ILB contains a strong atmospheric component. In this section we turn our attention to non-atmospheric contributions to the ILB, specifically zodiacal scattered light and scattered moonlight. Based on the estimates from our models, these contributions are small. However, some of the sky frames were taken near the ecliptic plane and/or at small lunar distances, where these contributions may be quite large. Thus, we determined the level of contribution from these components to the ILB in our data. ZSL is discussed in this section and moonlight is discussed in the next section.

Here we will assume that the strong atmospheric component is instrumentally-scattered OH emission. Then we determine the contribution from instrumentally-scattered OH emission, ZSL and scattered moonlight to the ILB by exploiting the variation of the ILB with zenith distance, time after sunset, ecliptic latitude, and chiefly lunar distance to distinguish the various components. The instrumentally-scattered OH component was modelled as

$$I_{\text{OH}}(t, z) = I_{0,\text{OH}} I_0(t) X_1(z), \quad (16)$$

where $I_{0,\text{OH}}$ is an overall scaling constant, $X_1(z)$ is the van Rhijn factor and $I_0(t)$ is the piecewise linear model to the aggregate OH emission data from all 5 nights listed in Table 2 where we separately fitted a linear model the data before and after 7.5 hr after sunset. The ZSL and moonlight components were modelled using Equations 7 and 13, respectively. We determined the best-fitting $I_{0,\text{OH}}$, $I_{0,\text{ZSL}}$ and $I_{0,\text{moon}}$ values and their standard errors using NONLINEAR-MODELFIT in MATHEMATICA constraining the parameter values to be real and positive. The analysis yielded $I_{0,\text{OH}} = 500 \pm 150 \text{ photons s}^{-1} \text{ m}^{-2} \mu\text{m}^{-1} \text{ arcsec}^{-2}$, $I_{0,\text{ZSL}} = 4 \pm 4$ and $I_{0,\text{moon}} = 30 \pm 3$.

Based on the ZSL model of Ellis & Bland-Hawthorn (2008) and previous estimates of ZSL in the H band (Con-

tent 1996), the magnitude and the variation of the ZSL component with ecliptic latitude over the range covered by our sample ($\approx 40 \text{ photons s}^{-1} \text{ m}^{-2} \mu\text{m}^{-1} \text{ arcsec}^{-2}$) are too small to reliably measure this component by model fitting, which relies on the variation with ecliptic latitude to distinguish the ZSL component from other contributions to the ILB. Thus, we adopt the ZSL model of Ellis & Bland-Hawthorn (2008) and subtract the expected ZSL contribution from the ILB and fit the ZSL-subtracted ILB for OH and moonlight.

5.2.3 Scattered moonlight

Fitting the ZSL-subtracted ILB for OH and moonlight using NONLINEAR-MODELFIT in MATHEMATICA as before yields the best-fitting values of $I_{0,\text{OH}} = 620 \pm 40 \text{ photons s}^{-1} \text{ m}^{-2} \mu\text{m}^{-1} \text{ arcsec}^{-2}$ and $I_{0,\text{moon}} = 30 \pm 3$. In other words, the moonlight component is unaffected by the estimate of ZSL and is ≈ 30 times larger than expected based on expected contribution from extrapolated from the V band measurements of Krisciunas & Schaefer (1991). Figure 8 shows the moonlight component versus lunar distance. Moonlight is taken to be the difference between the ZSL-subtracted ILB and the best estimate of the OH component using the best-fitting value of $I_{0,\text{OH}}$ stated above. The solid and dashed curves correspond to the I_{moon} curves with $\lambda = 1.520 \mu\text{m}$, $z_{\text{sky}} = 0 \text{ deg}$, $z_{\text{moon}} = \rho$, and lunar phase angle $\alpha = -80, -118 \text{ deg}$, respectively, scaled by the best-fitting $I_{0,\text{moon}}$ value listed above.

The data agree with the essential features of the Krisciunas & Schaefer (1991) model. We were able to reliably measure the moonlight component due to the 3 data points with $\rho \lesssim 11 \text{ deg}$, which have moonlight components that are sufficient large ($\gtrsim 300 \text{ photon s}^{-1} \text{ m}^{-2} \mu\text{m}^{-1} \text{ arcsec}^{-2}$) and change by a significant amount with ρ such that the model fitting procedure easily distinguishes the moonlight component from the OH component. At $\rho > 60 \text{ deg}$, the moonlight component is very small ($\lesssim 30 \text{ photon s}^{-1} \text{ m}^{-2} \mu\text{m}^{-1} \text{ arcsec}^{-2}$) and the scatter is simply a reflection of the scatter in the atmospheric component.

Our result indicates that scattered moonlight is much more significant in the H band than previously believed (Sullivan & Simcoe 2012). This has significant implica-

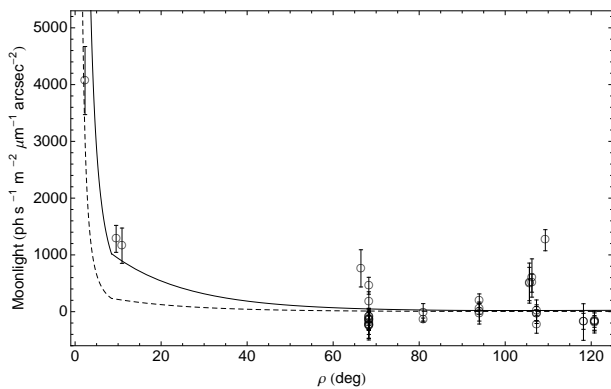


Figure 8. The scattered moonlight component of the ZSL-subtracted ILB as function of lunar distance. The solid and dashed curves correspond to the I_{moon} curves with $\lambda = 1.520 \mu\text{m}$, $z_{\text{sky}} = 0 \text{ deg}$, $z_{\text{moon}} = \rho$, and lunar phase angle $\alpha = -80, -118 \text{ deg}$, respectively, scaled by the best-fitting $I_{0,\text{moon}}$ value when fitting the ZSL-subtracted ILB for instrumentally-scattered OH and scattered moonlight. The 3 points at $\lesssim 11 \text{ deg}$ contain a significant amount of moonlight ($\gtrsim 300 \text{ photon s}^{-1} \text{ m}^{-2} \mu\text{m}^{-1} \text{ arcsec}^{-2}$) giving a reliable estimate even amongst the large scatter in the atmospheric component of the ILB.

tions for the allocation of observing time for the most demanding NIR programmes. For a given lunar phase angle, we computed the minimum lunar distance such that the contribution from scattered moonlight is no more than $100 \text{ photon s}^{-1} \text{ m}^{-2} \mu\text{m}^{-1} \text{ arcsec}^{-2}$ assuming $\lambda = 1.52 \mu\text{m}$, $z_{\text{sky}} = 0 \text{ deg}$ and $z_{\text{moon}} = \rho$. The result is shown in Figure 9. NIR programmes conducted during bright-grey time ($|\alpha| \gtrsim 30 \text{ deg}$) should make observations at a minimum lunar distance of $\rho \gtrsim 80 \text{ deg}$ to reduce the background from scattered moonlight.

5.3 Absolute interline background

Above we used the variability of the interline background measured at $1.520 \mu\text{m}$ to determine the presence of non-thermal atmospheric emission, zodiacal scattered light and scattered moonlight in the ILB. Now we turn our attention to the absolute brightness of the ILB under the darkest conditions. The ILB is certainly dominated by atmospheric emission component (either line emission scattered by the instrument or continuum) and low airmass observations will yield the lowest background. The ILB also decreases later in the night. For large lunar phase angles moonlight is absent at large angular distances. While we were unable to measure the ZSL component in our data, the ZSL model shows more ZSL near the ecliptic plane. Thus, we considered 12 sky frames with $\rho > 60 \text{ deg}$, $|b| > 10 \text{ deg}$, $X_2 < 1.2$, and $t > 6 \text{ hr}$. The mean and standard deviation of the ILB in these 12 sky frames gives $560 \pm 130 \text{ photon s}^{-1} \text{ m}^{-2} \mu\text{m}^{-1} \text{ arcsec}^{-2}$.

Our measured value is similar to the measurements of Sullivan & Simcoe (2012) and Maihara et al. (1993) at $1.665 \mu\text{m}$ at $R = 6000$ and $R = 17,000$, respectively, without OH suppression. This suggests that the ILB in their spectra and ours is the same, hence the suppression of the 103 brightest OH lines is not affecting the ILB as modelled by Ellis & Bland-Hawthorn (2008) and the ILB is domi-

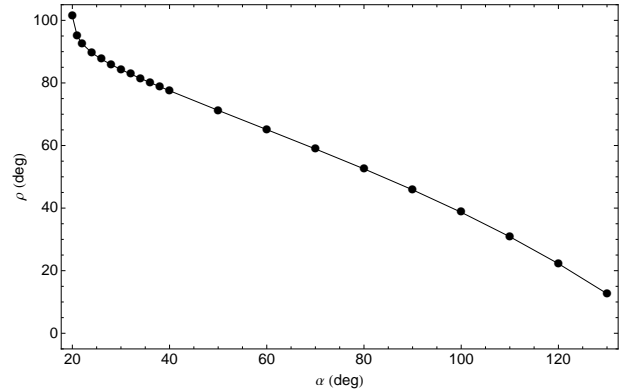


Figure 9. The lunar distance (ρ) where scattered moonlight contributes $\approx 100 \text{ photon s}^{-1} \text{ m}^{-2} \mu\text{m}^{-1} \text{ arcsec}^{-2}$ for various lunar phase angles (α) assuming $\lambda = 1.520 \mu\text{m}$, $z_{\text{sky}} = 0 \text{ deg}$ and $z_{\text{moon}} = \rho$. We have used the best-fitting $I_{0,\text{moon}}$ value when fitting the ZSL-subtracted ILB for instrumentally-scattered OH and scattered moonlight.

nated by emission from unsuppressed atmospheric emission (OH or other). This would also explain the lack of interline background reduction when comparing the control fibre to the OH suppressed fibres of GNOSIS. However, we remind the reader that these observations were detector noise-dominated and it is possible that there is an ILB reduction but we are unable to observe it amongst the detector noise. In any case, it is difficult to form a compelling argument at this point considering our ILB measurement was made at a different wavelength as we were unable to measure it at $1.665 \mu\text{m}$ due to contamination by instrumental thermal emission. A direct comparison at $1.665 \mu\text{m}$ with OH suppression fibres in a regime that is sky background-limited is left for future work.

6 SUMMARY

We have analysed 19 hr of H band observations taken with GNOSIS, the first OH suppression unit to utilise OH suppression fibres, with the IRIS2 spectrograph at the AAT. These data include 45 sky frames covering a range of sky positions and lunar conditions. From these data, we examined the spatial and temporal behaviours of OH and O_2 emission and the interline background to determine the nature of the ILB measured at $1.520 \mu\text{m}$ when using the first generation of OH suppression fibres at $R \approx 2400$. This analysis is a critical step in the development of OH suppression fibres, which may potentially impact astronomy at the level of adaptive optics or greater.

We studied the temporal behaviour of OH emission by measuring the average of 17 lines at $\lambda > 1.7 \mu\text{m}$ and found that it is best modelled by a gradual linear decrease the first half of the night followed by a gradual linear rise during the second half of the night following the behaviour of the solar elevation angle. O_2 emission on the other hand, exhibits very rapid dimming after sunset as measured from the a-X $v=1-0$ line at $1.58 \mu\text{m}$.

For space-based observations, the dominant NIR background component is zodiacal scattered light. Unfortunately, given the large variability of the atmospheric component in

the ILB and the small ZSL variation with ecliptic latitude, we were unable to reliably measure ZSL in our data. We adopted the ZSL model of Ellis & Bland-Hawthorn (2008) and removed this component from the ILB before assessing the contribution from moonlight.

The contribution from scattered moonlight in the H band is ≈ 30 times larger than expected based on a model extrapolated from the V band measurements of Krisciunas & Schaefer (1991) assuming the strong atmospheric component is instrumentally-scattered OH emission. Demanding NIR observations during low lunar phase angles ($|\alpha| \gtrsim 30$ deg) should be made at lunar distances $\rho \gtrsim 80$ deg if the background contribution is not to exceed $100 \text{ photons s}^{-1} \text{ m}^{-2} \mu\text{m}^{-1} \text{ arcsec}^{-2}$. We were able to reliably measure the moonlight component due to 3 sky frames with $\rho < 11$ deg which have a significant amount of moonlight and exhibited a large change with ρ making it easy for the model fitting process to distinguish the moonlight component from the atmospheric component of the ZSL-subtracted ILB.

Although moonlight dominates the interline background at very small lunar distances the background when using OH suppression fibres is otherwise dominated by non-thermal atmospheric emission, either line emission scattered by the instrument or continuum. The ILB exhibits the characteristic $X[z(t)]$ behaviour expected of emission from an atmospheric molecule when following the same field throughout the night. Additionally, the temporal behaviour of the ILB is similar to that of OH and O_2 with the dimming of the ILB early in the night being intermediate between the slow rate of OH and the fast rate of O_2 . There is also a strong linear correlation between the ILB and OH as well as the ILB and O_2 . This suggests that the ILB contains atmospheric emission from multiple molecules with time dependences like OH and like O_2 . It is plausible that the ILB contains OH given that the ILB was measured near several OH lines, but there are no O_2 transitions in the ILB measurement region although O_2 -like molecules may contribute.

The absolute interline background is $560 \pm 130 \text{ photons s}^{-1} \text{ m}^{-2} \mu\text{m}^{-1} \text{ arcsec}^{-2}$ at $1.520 \mu\text{m}$ under dark conditions. This value is similar to previous measurements without OH suppression suggesting that the suppression with the current grating design does not affect the ILB and it is dominated by emission from unsuppressed atmospheric emission. There is some uncertainty regarding this conclusion given that the GNOSIS observations are detector noise-dominated and the ILB comparison was made a two different wavelengths. We are currently designing an optimised fibre-fed spectrograph, called PRAXIS, with a high performance, low noise $1.7 \mu\text{m}$ cutoff Hawaii-2RG detector to be used with the GNOSIS OH suppression unit to provide sky background-limited data with significantly reduced thermal noise (Horton et al. 2012). If no ILB reduction is seen there, then it will be clear that unsuppressed atmospheric emission is responsible for the ILB. In this case, an ILB reduction may still be possible with improved grating design.

For example, there is evidence unsuppressed OH lines originally thought to be very weak are responsible for the lack of ILB reduction. This could certainly account for the observed linear correlation between the ILB and OH. The simulations Ellis & Bland-Hawthorn (2008) showed an ILB

reduction when the sky is modelled according to the OH line list of Rousselot et al. (2000). Only the 103 brightest OH doublets needed to be suppressed because the other unsuppressed lines are so weak that they do not matter. However, the OH line list of Abrams et al. (1994) shows that some of the unsuppressed lines are much stronger, which would scatter more light into the interline regions. When using an updated OH line spectrum which is an amalgamation of Abrams et al. (1994) and Rousselot et al. (2000) giving precedence to Abrams et al. (1994) when a line occurs in both lists, the simulated spectrum is a better match to the observed GNOSIS spectrum. If this is the case, the more accurate model of the night sky may be used to determine the number of lines that need to be suppressed to achieve the desired ILB reduction. This highlights the fact that for proper sky suppression, accurate skyline positions and strengths are critical. New measurements of the OH lines are being carried out with high resolution spectra taken with CRIFES (CRYogenic high-resolution InfraRed Echelle Spectrograph) at the Very Large Telescope (Chris Lidman, private communication). Future grating designs will incorporate these new measurements in order to optimise the performance of OH suppression fibres for deep ground-based NIR spectroscopy.

ACKNOWLEDGMENTS

The GNOSIS team acknowledges funding by ARC LIEF grant LE100100164. CQT gratefully acknowledges support by the National Science Foundation Graduate Research Fellowship under Grant No. DGE-1035963. CQT would like to thank Robert Content for helpful discussion and comments, Renée Pelton, Billy Robbins, and Andrew Sheinis.

REFERENCES

- Abrams M. C., Davis S. P., Rao M. L. P., Engleman R., Jr., Brault J. W., 1994, *ApJS*, 93, 351
- Baker D. J., Stair A. T., Jr., 1988, *Physica Scripta*, 37, 611
- Bates D. R., Nicolet M., 1950, *J. Geophysical Research*, 55, 301
- Bland-Hawthorn J., Veilleux S., Cecil G. N., Putman M. E., Gibson B. K., Maloney P. R., 1998, *MNRAS*, 299, 611
- Bland-Hawthorn J., Englund M., Edvell G., 2004, *Optics Express*, 12, 5902
- Castelli F., Kurucz R. L., 1994, *A&A*, 281, 817
- Content R., 1996, *ApJ*, 464, 412
- Cox A. N., 2000, in Arthur N. C., ed., *Allen's Astrophysical Quantities*, 4th edn. AIP Press; Springer, New York
- Davies R. I., 2007, *MNRAS*, 375, 1099
- Dufay M., 1951, *Publications of the Observatoire Haute-Provence*, 2
- Ellis S. C., Bland-Hawthorn J., 2008, *MNRAS*, 386, 47
- Ellis S. C. et al., 2012, *MNRAS*, 425, 1682
- Frey H. U., Mende S. B., Arens J. F., McCullough P. R., Swenson G. R., 2000, *Geophysical Research Letters*, 27, 41
- Garstang R. H., 1989, *PASP*, 101, 306
- Glazebrook K., Bland-Hawthorn J., 2001, *PASP*, 113, 197
- Horton A. J., Ellis S. C., Lawrence J. S., Bland-Hawthorn J., 2012, *Proc. SPIE*, 8450

- Kelsall T. et al., 1998, *ApJ*, 508, 44
Krisciunas K. et al., 1987, *PASP*, 99, 887
Krisciunas K., Schaefer B. E., 1991, *PASP*, 103, 1033
Leon-Saval S. G., Birks T. A., Bland-Hawthorn J., 2005, *Optics Letters*, 30, 2545
Llewellyn E. J., Long B. H., Solheim B. H., 1978, *Planetary and Space Science*, 26, 525
Maihara T., Iwamuro F., Yamashita T., Hall D. N., Cowie L. L., Tokunaga A. T., Pickles A., 1993, *PASP*, 105, 940
Meinel I. A. B., 1950, *ApJ*, 111, 555
Ramsay S. K., Mountain C. M., Geballe T. R., 1992, *MNRAS*, 259, 751
Rothman L. S. et al., 2009, *J. Quant. Spectrosc. Radiat. Transfer*, 110, 533
Rousselot P., Lidman C., Cuby J.-G., Moreels G., Monnet G., 2000, *A&A*, 354, 1134
Sharp R., Birchall M. N., 2010, *PASA*, 27, 91
Shimazaki T., Laird A. R., 1970, *JGR*, 75, 3221
Sullivan P. W., Simcoe R. A., 2012, *PASP*, accepted
Taylor M. J., Espy P. J., Baker D. J. et al., 1991, *Planet. Space Sci.*, 39, 1171
Tinney C. G. et al., 2004, *Proc. SPIE*, 5492, 998
Trinh C. Q. et al. 2012, *AJ*, accepted
Thompson R. I., Eisenstein D., Fan X., Rieke M., Kennicutt R. C., 2007, *ApJ*, 657, 669
Turnbull D. N., Lowe R. P., 1983, *Canadian Journal of Physics*, 61, 244
van Rhijn P. J., 1921, *Publications of the Kapteyn Astronomical Laboratory Groningen*, 31, 1
Yee J.-H., Niciejewski R. J., Luo M. Z., 1991, *Geophysical Research Letters*, 18, 1357